

Graph Neural Networks-based Hybrid Framework For Predicting Particle Crushing Strength

Tongya Zheng^{1,2}, Tianli Zhang³, Qingzheng Guan⁴, Wenjie Huang², Zunlei Feng³, Mingli Song^{2,*}, Chun Chen²

Abstract

Graph Neural Networks have emerged as an effective machine learning tool for multi-disciplinary tasks such as pharmaceutical molecule classification and chemical reaction prediction, because they can model non-euclidean relationships between different entities. Particle crushing, as a significant field of civil engineering, describes the breakage of granular materials caused by the breakage of particle fragment bonds under the modeling of numerical simulations, which motivates us to characterize the mechanical behaviors of particle crushing through the connectivity of particle fragments with Graph Neural Networks (GNNs). However, there lacks an open-source large-scale particle crushing dataset for research due to the expensive costs of laboratory tests or numerical simulations. Therefore, we firstly generate a dataset with 45,000 numerical simulations and 900 particle types to facilitate the research progress of machine learning for particle crushing. Secondly, we devise a hybrid framework based on GNNs to predict particle crushing strength in a particle fragment view with the advances of *state-of-the-art* GNNs. Finally, we compare our hybrid framework against traditional machine learning methods and the plain MLP to verify its ef-

*Corresponding author

Email addresses: doujiang_zheng@163.com (Tongya Zheng), zhangtianli@zju.edu.cn (Tianli Zhang), 11912051@zju.edu.cn (Qingzheng Guan), wjie@zju.edu.cn (Wenjie Huang), zunleifeng@zju.edu.cn (Zunlei Feng), brooksong@zju.edu.cn (Mingli Song), chenc@zju.edu.cn (Chun Chen)

¹Big Graph Center, College of Computer Science, Hangzhou City University

²College of Computer Science, Zhejiang University

³College of Software Technology, Zhejiang University

⁴Department of Civil Engineering, Zhejiang University

fectiveness. The usefulness of different features is further discussed through the gradient attribution explanation *w.r.t* the predictions. Our data and code are released at <https://github.com/doujiang-zheng/GNN-For-Particle-Crushing>.

Keywords: Graph Neural Networks, Model Explanation, Civil Engineering, Particle Crushing, Size Effect

1. Introduction

Graph, as an abstract data structure, describes the complex relationships among various entities, such as the billions of directed links between webpages on the Internet Page et al. (1999), the chemical bonds between atoms in the chemical engineering Gilmer et al. (2017), the COVID-19 spread between people in the social networks Chang et al. (2021). Recently, with the development of deep learning techniques LeCun et al. (2015), Graph Neural Networks (GNNs) Kipf and Welling (2017); Bronstein et al. (2017) have advanced the representation learning of graphs in multiple disciplinary tasks Gilmer et al. (2017); Vlassis et al. (2020); Zhang et al. (2023) by stacking non-linear graph convolution layers over the graph topology. In civil engineering, numerical simulations usually treat a particle as a combination of several randomly tessellated particle fragments Hu et al. (2022); de Bono and McDowell (2014); Fu et al. (2017); Cheng et al. (2004); Huilca et al. (2021), and investigate the mechanical behaviors of particles under the external load based on the breakage of fragment bonds, which motivates us to handle the particle prediction tasks with the *state-of-the-art* GNNs.

In the civil engineering, particles would break into several smaller fragments under the structural loads due to the surface flaws Ma et al. (2022) or the internal flaws Ma et al. (2014); Huilca et al. (2021); Griffith (1921), leading to the degradation of mechanical properties Lade et al. (1996); Nakata et al. (1999); Ovalle et al. (2014); Cantor et al. (2017), which could cause serious consequences such as the excessive and dangerous settlement of buildings Hardin et al. (1985); McDowell and Bolton (1998); Zhu and Zhao (2019a); Lade et al.

(1996); Nakata et al. (1999); Ovalle et al. (2014); Nader et al. (2019). Recent research of particle crushing has largely extended the investigation of particle crushing from a single particle McDowell and Amon (2000) to particles with different mechanical properties such as particle sizes Huang et al. (2014); Huilca et al. (2021), particle shapes Fu et al. (2017); Hu et al. (2022); Zhu and Zhao (2021), and particle morphology Sun et al. (2021); Wang et al. (2021); Ma et al. (2022). These dedicated heuristics of particle properties are summarized as morphology descriptors of particles in Wang et al. (2021), which can be divided into the form descriptors, the roundness descriptors, and the sphericity descriptors.

Despite the effectiveness of morphology descriptors, they are far away from the particle crushing mechanisms investigated by existing numerical simulation methods Hu et al. (2022); de Bono and McDowell (2014); Fu et al. (2017); Cheng et al. (2004); Huilca et al. (2021). These methods model a particle as a polyhedron of the connected fragments and obtain the particle states at each time step by solving the displacements of different fragments, which investigates particle crushing in a microscopic view instead of the morphology view. The simulated particle crushing process inspires us to model the particle as a connected fragment graph and advance the representation of particles from morphology descriptors to their internal mechanisms. Furthermore, unlike the machine learning community that has released various datasets, there lacks an open-source dataset of particle crushing, which significantly hinders the development of its machine learning research.

Therefore, we firstly provide an open-source large-scale particle crushing dataset of 45,000 particles by simulating the crushing process of a single rockfill particle under one-dimensional (1D) compression with the Non-Smooth Contact Dynamics (NSCD) method following Hu et al. (2022). The particle crushing dataset consists of 900 different particle types, with 20 different particle diameters, 15 different particle shapes, and 3 different compression axes. Each type of particle is randomly tessellated into multiple polyhedron fragments by the Neper Kun and Herrmann (1996); Nguyen et al. (2015); Quey et al. (2011) with

the specific diameter and shape. The tessellated particle is then compressed by two rigid parallel platens along the specific compression axis, following a DEM model with a three-dimensional bonded-cell method [Huillca et al. \(2021\)](#). The numerical model was implemented in the software LMGC90 [Dubois and Mozul \(2013\)](#), which is based on the non-smooth contact dynamics method [Rafiee et al. \(2008, 2011\)](#).

Secondly, we model the particle fragments as a connected fragment graph to utilize *state-of-the-art* machine learning tools for particle representation. The interacted fragments of a particle could be seen as a connected graph, where each fragment acts as a vertice and interacts with other fragments during the particle crushing process. The complex interaction between fragments could be learned by the emerging Graph Neural Networks (GNNs) [Bronstein et al. \(2017\)](#); [Kipf and Welling \(2017\)](#); [Xu et al. \(2019\)](#) with the large-scale particle crushing dataset. We are inspired by these encouraging applications of GNNs [Feng et al. \(2019\)](#); [Chang and Cheng \(2020\)](#); [Schulte-Sasse et al. \(2021\)](#); [Ying et al. \(2021\)](#); [Yang et al. \(2020\)](#); [Zhang et al. \(2021\)](#); [Addanki et al. \(2021\)](#); [Vlassis et al. \(2020\)](#) to build a GNNs-based hybrid framework to combine GNNs based on the fragment graph with MLP based on the dedicated morphology descriptors, predicting the characteristic crushing strength of particles on the newly given particles in the testing set.

Finally, we have conducted experiments to examine the prediction performance of our proposed hybrid framework, the effectiveness of different components, and the attributions of the calculated features. To validate the generalization ability of different methods, we propose three kinds of testing sets to construct three different tasks, which are split by the diameter, shape, and compression axis, respectively. We have calculated geometric descriptors as described in [Huang et al. \(2014\)](#); [Huillca et al. \(2021\)](#); [Fu et al. \(2017\)](#); [Hu et al. \(2022\)](#); [Zhu and Zhao \(2021\)](#); [Sun et al. \(2021\)](#) and compared five traditional machine learning methods [Pedregosa et al. \(2011\)](#); [Chen and Guestrin \(2016\)](#); [Ke et al. \(2017\)](#) (denoted as non-Deep methods) against a bunch of Deep Neural Networks (DNNs) including three kinds of *state-of-the-art* GNNs [Feng et al.](#)

(2019); Xu et al. (2019); Yang et al. (2020), where GNNs are implemented using our hybrid framework. The contributions of the morphology descriptors for MLP and the node and edge features for GNNs are further verified through the ablation studies on three GNNs across three different tasks. The common and individual patterns of the three tasks are analyzed through the visualization results of feature attributions based on the gradient norms.

The main contributions can be summarized as follows:

- We generate a large-scale particle crushing dataset to facilitate the machine learning research of this field, comprising 45,000 numerical simulations with 900 different particle types.
- We build a GNNs-based hybrid framework to model a particle with elementary cell interactions and its overall morphology descriptors for predicting the particle crushing strength across three different tasks.
- We have conducted elaborate comparison experiments and ablation studies to investigate the effectiveness of GNNs, particle morphology descriptors, and features for nodes and edges. We further visualize the common and individual patterns through the saliency map of different features.

2. Related Works

2.1. Graph Neural Networks

Graph Neural Networks (GNNs) have shown their powerful prediction abilities on the non-grid data and have been applied to various fields such as Recommendation Ying et al. (2018), traffic flow prediction Yu et al. (2018), and molecular classification Gilmer et al. (2017); Xu et al. (2019); Yang et al. (2020); Ying et al. (2021). A graph is defined by a node set $V = \{v_1, \dots, v_n\}$ and an associated edge set $E = \{e_1, \dots, e_m\}$, where e_1 connects a pair of adjacent fragments v_i and v_j . The message-passing paradigm Gilmer et al. (2017) describes GNNs in a microscopic view that each node v_i receives the messages from its

neighbors $v_j \in \mathcal{N}(v_i)$ and updates its representation based on these messages, written as:

$$\begin{aligned} \mathbf{m}_i^k &= \sum_{v_j \in \mathcal{N}(v_i)} \mathbf{M}_k(\mathbf{h}_i^k, \mathbf{h}_j^k, \mathbf{e}_{ij}), \\ \mathbf{h}_i^{k+1} &= \mathbf{U}_k(h_i^k, \mathbf{m}_i^k), \end{aligned} \tag{1}$$

where v_i updates from \mathbf{h}_i^k of the k -th layer to \mathbf{h}_i^{k+1} of $k + 1$ -th layer based on the message function \mathbf{M}_k and the update function \mathbf{U}_k . The obtained node representation \mathbf{h}_i can be used for various tasks such as node classification [Kipf and Welling \(2017\)](#) and link prediction [Ying et al. \(2018\)](#). It requires a readout function to generate a representation vector for the whole graph G for graph-level tasks like molecular classification [Gilmer et al. \(2017\)](#); [Xu et al. \(2019\)](#); [Yang et al. \(2020\)](#); [Ying et al. \(2021\)](#), written as

$$\mathbf{h}_G = \mathbf{R}(\{\mathbf{h}_i^K | v_i \in V\}), \tag{2}$$

where K is the number of neural network layers. Furthermore, GNNs have proved their applications in various fields, such as predicting the deformation of 3D objects given the 3D meshed data points [Feng et al. \(2019\)](#), generating artificial building structures to alleviate the efforts of experts [Chang and Cheng \(2020\)](#), predicting the HOMO-LUMO energy gap of molecules given their 2D molecular graphs [Schulte-Sasse et al. \(2021\)](#); [Ying et al. \(2021\)](#); [Yang et al. \(2020\)](#); [Zhang et al. \(2021\)](#); [Addanki et al. \(2021\)](#), and predicting the homogenized responses of polycrystals [Vlassis et al. \(2020\)](#).

2.2. Particle Crushing

McDowell *et al.* [McDowell and Amon \(2000\)](#) have found that the particle crushing strength of geometrically similar particles follows a Weibull distribution, written as

$$P_s = \exp \left[- \left(\frac{d_s}{d_0} \right)^3 \left(\frac{\sigma}{\sigma_0} \right)^m \right], \tag{3}$$

where P_s is the breakage ratios under the corresponding load, d_0 and σ_0 are the characteristic diameter and crushing strength, respectively. The survival probability of a batch of 50 particles with the same geometry is drawn in [Fig. A.6](#),

sorting by the normalized particle strength, where $m = 9.690$ is the Weibull modulus and indicates the variability of the particle crushing distribution. The characteristic particle strength is thus scaled to 1.0 of the horizontal axis and corresponds to the 37% survival probability of the vertical axis. Existing particle crushing theories [McDowell and Amon \(2000\)](#); [Sun et al. \(2021\)](#); [Wang et al. \(2021\)](#) derive a closed-form formula to describe the size effects of particles with different diameters. However, firstly, their various theories have been proposed from different perspectives and lacked a consensus on particle crushing behaviors. Secondly, our experimental results of the non-Deep methods and DNNs in [Tab. 3](#) reveal that particle morphology descriptors play a vital role in the generalization of predicting the particle crushing strength while existing theories are mostly based on the particle diameter. Thirdly, generalizing the predictions for more conditions like particle shapes and compression axes requires a constitutive model to describe the particle from different viewpoints. Therefore, we are motivated to model the fragment connection of the particle with Graph Neural Networks (GNNs), which offer natural modeling for the fragment graph.

3. Method

As shown in [Fig. 1](#), we first conduct numerical simulations for 900 particle types with different diameters, shapes, and compression axes to measure the characteristic particle crushing strength. Secondly, we build a hybrid framework to combine the *state-of-the-art* GNNs with the MLP network to predict the strength of the Diameter, Shape, and Axis tasks and validate the generalization ability of DNNs and GNNs. Lastly, we quantitatively attribute the input contributions to the predictions and analyze the common and individual patterns of the three tasks.

3.1. Dataset Generation

To overcome the limitations of small-scale datasets of existing researches [Huang et al. \(2014\)](#); [Huillca et al. \(2021\)](#); [Fu et al. \(2017\)](#); [Hu et al. \(2022\)](#); [Sun et al.](#)

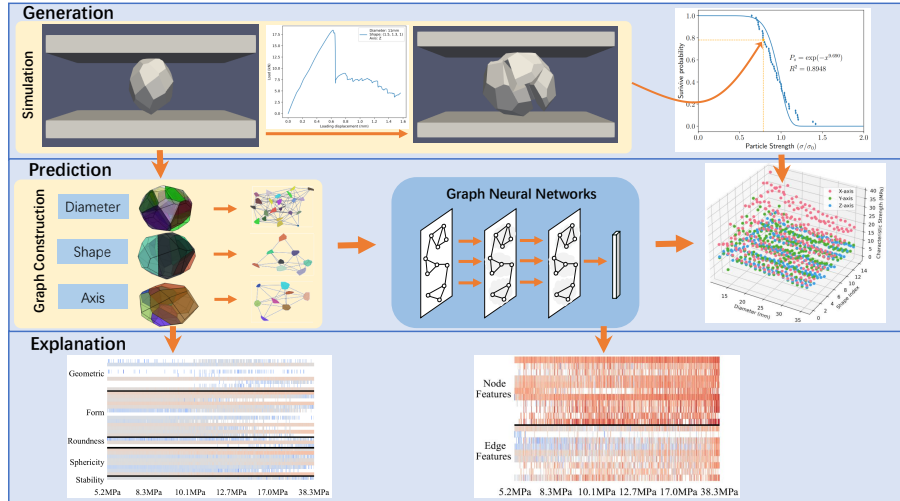


Figure 1: The pipeline of our work consists of three parts, where the **generation** part means the large-scale dataset, the **prediction** part means the graph construction of each particle and the hybrid framework for particle crushing strength, and the **explanation** part visualizes the importance of different features w.r.t their gradient magnitudes.

(2021); Zhu and Zhao (2019b); Wang et al. (2021); Nguyen et al. (2015), we firstly generate 45,000 particles and simulate their crushing processes based on numerical simulations Hu et al. (2022); de Bono and McDowell (2014); Fu et al. (2017); Cheng et al. (2004); Huilca et al. (2021). As shown in Tab. 1, there are 900 different particle types in total, the Cartesian product of 20 different particle diameters, 15 different scale shapes in the (X, Y, Z) axes, and 3 different compression axes under one-dimensional compression. Each type contains 50 particle crushing tests McDowell and Amon (2000); Hu et al. (2022); Sun et al. (2021) to estimate the characteristic crushing strength of the specific particle type, where each test is based on a randomly tessellated particle. The comprehensive large-scale dataset can measure the generalization ability of the *state-of-the-art* machine learning methods from the three aspects of diameter, shape, and axis, and examine the feature attributions with respect to the predictions of particle crushing strength based on the well-trained models.

The top row of Fig. 1 describes the crushing process of an example particle

Table 1: Configuration of particle crushing dataset. The *italic* font refers to the testing settings.

Dimension	Setting
Diameter (mm)	11.86, 13.10, 14.35, 15.60, 16.85, 18.10, 19.34, 20.59, 21.84, 23.09, 24.34, 25.58, 26.83, <i>28.08</i> , <i>29.33</i> , <i>30.58</i> , <i>31.82</i> , <i>33.07</i> , <i>34.32</i> , <i>35.57</i>
Scale Shape (X, Y, Z)	(1,1,1), (<i>1/0.95,0.95,1</i>), (1/0.9,0.9,1), (1.1,1.1,1), (<i>1.25,1.21/1.25,1</i>), (1.21/0.9,0.9,1), (1.2,1.2,1), (<i>1.25,1.44/1.25,1</i>), (1.5,1.44/1.5,1), (1.3,1.3,1), (<i>1.25,1.69/1.25,1</i>), (1.5,1.69/1.5,1), (1.4,1.4,1), (<i>1.25,1.96/1.25,1</i>), (1.5,1.96/1.5,1)
Compression Axis	X-axis, <i>Y-axis</i> , Z-axis

compressed by two plates, where the particle stress drops drastically from the peak when the particle breaks into pieces [McDowell and Amon \(2000\)](#); [Huillca et al. \(2021\)](#) as shown in the stress curve with respect to the time step. The particle strength is computed by $\sigma = F_c/d^2$, where F_c is the peak stress and d is the distance between two plates, serving as a data point in a batch of particle crushing tests of a specific particle type, which is given the specific diameter, shape, and axis. As shown in the top right plot of [Fig. 1](#), the batch of particle crushing tests fits the Weibull statistics by sorting the particle strength in an ascending order, where the particle strength is normalized by the characteristic particle strength σ_0 at 37% survival probability. When increasing the particle strength, the survival probability P_s of the batch of particles decreases exponentially fast at $P_s = \exp(-x^{9.690})$ with $R^2 = 0.8948$, where the Weibull modulus 9.690 depicts the sharpness of the strength-probability curve. As shown in previous researches [Huang et al. \(2014\)](#); [Huillca et al. \(2021\)](#); [Fu et al. \(2017\)](#); [Hu et al. \(2022\)](#); [Sun et al. \(2021\)](#); [Zhu and Zhao \(2019b\)](#); [Wang et al. \(2021\)](#); [Nguyen et al. \(2015\)](#), when individually and jointly varying the conditions of diameter, shape, and axis, different particle types exhibit distinct mechanical

properties. Therefore, it is of vital importance to generalize prediction models from the comprehensive training set to the unseen testing set, capturing the macroscopic properties of granular materials.

In the numerical simulation of a particle compression test, a randomly tessellated particle by Neper [Kun and Herrmann \(1996\)](#); [Nguyen et al. \(2015\)](#); [Quey et al. \(2011\)](#) is firstly meshed by Gmsh [Geuzaine and Remacle \(2009\)](#) and then compressed by two rigid plates using LMGC90 [Dubois and Mozul \(2013\)](#) with a Non-Smooth Contact Dynamics (NSCD) [Jean \(1999\)](#); [Rafiee et al. \(2008, 2011\)](#) method. Firstly, a batch of 50 particles is randomly tessellated into fragments for a specific particle type following the Voronoi tessellation algorithm [Quey et al. \(2011\)](#) to simulate the fragment size distributions of realistic rockfill particles. Secondly, the numerical model implemented by LMGC90 [Dubois and Mozul \(2013\)](#) solves the displacements of particle fragments by computing the contact forces of each body following the Signorini-Coulomb condition [Jean and Moreau \(1992\)](#); [Moreau \(1988\)](#) and the Cohesive Zone Model (CZM) model [Hu et al. \(2022\)](#); [Huillca et al. \(2021\)](#). The simulated particle breaks into pieces when the CZM bonds of particle fragments break due to external loadings. As shown in Fig. 1, the peak force of particle crushing is recorded when a drastic drop of more than 35% of the force is observed in the time step-force curve, indicating the particle breakage phenomenon [Wang et al. \(2021\)](#); [Huillca et al. \(2021\)](#); [Hu et al. \(2022\)](#).

Finally, we summarize the parameter settings of the particle generation process as follows. In the particle tessellation process, the number of particle fragments is initialized by 8 with a diameter of 11.86 mm and increases cubically from 8 to 216 with respect to the diameter, ensuring the constant cell density following that the internal flaws of particles increase with the increasing particle size [Griffith \(1921\)](#). In the particle crushing process, the friction coefficient between the rigid plates and the particle is set to 0.3 with a constant vertical velocity of the upper plate, the time step is set to 5×10^{-4} s, and the CZM parameters of particles are calibrated by the commonly adopted Brazilian splitting test [Jiang and Meng \(2018\)](#); [Yu and Yin \(2004\)](#). To examine the generalization

ability of machine learning methods, the ratios of the testing set are set to 7/20, 5/15, 1/3 in terms of different diameters, shapes, and axes, respectively.

3.2. Problem Setup of Predicting Particle Crushing Strength

Given a detailed 3D mesh of a particle and its fragments, the regression task of predicting the characteristic particle crushing strength σ_0 is written as

$$\arg \min_{\mathcal{F}} \sum_{\mathbf{x} \in \mathbf{X}, \mathbf{y} \in \mathbf{Y}} \|\mathbf{y} - \mathcal{F}(\mathbf{x})\|_2 + \lambda \Omega(\mathcal{F}), \quad (4)$$

where \mathbf{x}, \mathbf{y} are the particle and its σ_0 , \mathbf{X}, \mathbf{Y} are the sets of input particles and their prediction labels, \mathcal{F} is a machine learning method, the task is optimized by the Mean Squared Error (MSE) loss between the labels \mathbf{y} and the predictions $\mathcal{F}(x)$ and a regularization term $\Omega(\mathcal{F})$ reducing the complexity of \mathcal{F} , and λ is a tunable coefficient.

Based on the 3D mesh \mathbf{x} of a particle, we follow the particle morphology descriptors of existing researches [Blott and Pye \(2008\)](#); [Bagheri et al. \(2015\)](#); [Huang et al. \(2020\)](#); [Domokos et al. \(2015\)](#); [Pouranian et al. \(2020\)](#); [Zhao and Wang \(2016\)](#); [Yang et al. \(2017\)](#); [Zheng et al. \(2021\)](#); [Zhang et al. \(2016\)](#), which have shown dominant impacts on the crushing strength. As summarized by Wang *et al.* [Wang et al. \(2021\)](#), there are thirty-five particle morphology descriptors, including nine geometric characteristics [Wang et al. \(2021\)](#), thirteen form descriptors [Blott and Pye \(2008\)](#); [Bagheri et al. \(2015\)](#); [Huang et al. \(2020\)](#); [Domokos et al. \(2015\)](#), three roundness descriptors [Pouranian et al. \(2020\)](#); [Huang et al. \(2020\)](#); [Zhao and Wang \(2016\)](#), nine sphericity descriptors [Blott and Pye \(2008\)](#); [Pouranian et al. \(2020\)](#); [Yang et al. \(2017\)](#); [Zheng et al. \(2021\)](#); [Huang et al. \(2020\)](#); [Zhang et al. \(2016\)](#), and one instability descriptor [Wang et al. \(2021\)](#). These particle morphology descriptors are fed into traditional machine learning methods for predicting the particle crushing strength, including Linear Regression, Ridge Regression, Random Forest (RF), XGBoost (XGB) [Chen and Guestrin \(2016\)](#), and LightGBM (LGB) [Ke et al. \(2017\)](#). The former two are linear methods, and the latter three are ensemble tree-based methods, which can capture complex patterns of morphology

descriptors. We further apply a Multi-Layer Perceptron (MLP) to model the multivariate relationships of various morphology descriptors, which serves as the baseline method to verify the effectiveness of deep learning methods and Graph Neural Networks (GNNs).

3.3. GNNs-based Hybrid Framework

Despite their significant efforts, morphology descriptors mostly work based on insightful observations of researchers and hardly take the internal structure of particles into account, which plays an essential role in the particle crushing process as shown in previous literatures [McDowell and Bolton \(1998\)](#); [Daouadji et al. \(2001\)](#); [Russell and Khalili \(2004\)](#); [Tengattini et al. \(2016\)](#); [Ma et al. \(2022\)](#). In a numerical simulation, a particle is divided into multiple fragments randomly [Quey et al. \(2011\)](#) and breaks into pieces due to the breakage of the CZM bonds of fragments [Hu et al. \(2022\)](#). The mutual relationships of particle fragments thus influence the particle crushing behaviors significantly, which can doubtlessly help the predictions if the internal structure is considered.

Let $V = \{v_1, \dots, v_n\}$ be the fragment set of a particle, where v_1 is one of the fragments, and n is the number of fragments. The mutual relationships of V can be well described by an edge set $E = \{e_1, \dots, e_m\}$, where e_1 connects a pair of adjacent fragments v_i and v_j . The consequent fragment graph $G = \{V, E\}$ describes the internal structure of a particle, which can output the latent representation of the particle using *state-of-the-art* GNNs [Feng et al. \(2019\)](#); [Xu et al. \(2019\)](#); [Yang et al. \(2020\)](#). As shown in Fig. 1, GNNs use the fragment graph of particles as the inputs and predict the corresponding particle crushing strength σ_0 in terms of different diameters, shapes, and axes, which can be written as

$$\arg \min_{\mathbf{g}} \sum_{\mathbf{x} \in \mathbf{X}, \mathbf{y} \in \mathbf{Y}} \|\mathbf{y} - \mathbf{g}(\mathbf{x}, G)\|_2 + \lambda \Omega(\mathbf{g}), \quad (5)$$

where \mathbf{g} is one kind of GNNs. On the one hand, GNNs can summarize the latent representations from the fragment level to the particle level by aggregating neighborhood information iteratively with the fragment graph, complementing the missing microscopic interactions of fragments of particle morphology

Table 2: The distribution of particle crushing strength in the testing sets.

Quantile	Diameter (MPa)	Shape (MPa)	Axis (MPa)
min	5.09	5.54	5.09
25%	8.05	9.09	7.49
50%	10.13	11.27	8.80
75%	13.38	14.70	10.04
max	21.71	33.34	17.62

descriptors. On the other hand, dedicated efforts for particle morphology descriptors can largely alleviate the task difficulty of predicting particle crushing strength σ_0 , which is verified by Fig. 2. Therefore, we build a hybrid framework of a GNN and an MLP by summing their predictions to advance the training of GNNs, written as $\mathbf{g}' = \mathbf{g}(\mathbf{x}, G) + \text{MLP}(\mathbf{x})$.

We further prepare eleven node features and nine edge features for the fragment graph to characterize the internal states of particles, where a node is a particle fragment and an edge is the interaction between a pair of fragments. Following Vlassis *et al.* Vlassis et al. (2020), the states of a node are represented by its volume, its external area, diameter, the number of its external faces, the number of its neighborhood fragments, the 3D coordinates of its centroid, and its three Euler angles, which are computed by its mesh file generated by Neper Quey et al. (2011). Similarly, the edge states are represented by the contact area of fragments, the number of lines of the contact area, the maximum length of the contact area, the 3D coordinates of its centroid, and its three Euler angles. These node and edge features are then fed into GNNs for the latent representations of particles.

4. Experiment

4.1. Performance Comparison

We split different testing sets of different diameters, shapes, and axes to examine the task difficulty and generalization ability of methods. The com-

Table 3: Particle crushing prediction performance.

	Diameter		Shape		Axis	
	MAE (MPa)	RMSE (MPa)	MAE (MPa)	RMSE (MPa)	MAE (MPa)	RMSE (MPa)
Linear	3.961 ± 0.000	4.511 ± 0.000	2.266 ± 0.000	2.924 ± 0.000	2.693 ± 0.000	3.259 ± 0.000
Ridge	2.725 ± 0.000	3.290 ± 0.000	2.271 ± 0.000	2.950 ± 0.000	2.666 ± 0.000	3.223 ± 0.000
RF	1.084 ± 0.011	1.486 ± 0.012	1.140 ± 0.007	1.591 ± 0.013	2.434 ± 0.035	3.625 ± 0.039
XGB	0.810 ± 0.000	1.084 ± 0.000	1.025 ± 0.000	1.601 ± 0.000	1.451 ± 0.000	2.120 ± 0.000
LGB	0.881 ± 0.000	1.207 ± 0.000	1.047 ± 0.000	1.428 ± 0.000	1.762 ± 0.000	2.534 ± 0.000
MLP	0.771 ± 0.023	1.032 ± 0.024	0.935 ± 0.029	1.316 ± 0.056	0.814 ± 0.079	1.197 ± 0.101
MeshNet	0.719 ± 0.054	0.958 ± 0.048	1.027 ± 0.046	1.546 ± 0.053	0.731 ± 0.092	1.105 ± 0.122
GIN	0.719 ± 0.083	0.951 ± 0.070	0.910 ± 0.051	1.368 ± 0.095	0.746 ± 0.065	1.204 ± 0.054
ExpC	0.709 ± 0.025	0.944 ± 0.043	0.883 ± 0.036	1.388 ± 0.047	0.728 ± 0.031	1.079 ± 0.036

Table 4: The p-values of ExpC and other DNNs under two-sided t-test.

	Diameter	Shape	Axis
MLP	0.0035	0.0372	0.0531
MeshNet	0.7191	0.0006	0.9443
GIN	0.8038	0.3681	0.5929

pared methods include the *state-of-the-art* machine learning methods (denoted as non-Deep methods) [Pedregosa et al. \(2011\)](#); [Chen and Guestrin \(2016\)](#); [Ke et al. \(2017\)](#) and the *state-of-the-art* Deep Neural Networks (DNNs) [Feng et al. \(2019\)](#); [Xu et al. \(2019\)](#); [Yang et al. \(2020\)](#), aims at validating whether DNNs are superior to non-Deep methods and whether GNNs are superior to other DNNs. For three tasks of the Diameter, Shape, and Axis, we have tried numerous hyper-parameter settings of methods for a fair comparison of prediction ability and stability, where each setting takes 5 runs of fixed random seeds for reproducibility, as listed in Tab. C.9, Tab. C.10, and Tab. C.11. For non-Deep methods, there are 15 runs for Linear Regression, 60 runs for Ridge Regression, 675 runs for Random Forest, 5625 runs for XGBoost [Chen and Guestrin \(2016\)](#), and 5625 runs for LightGBM [Ke et al. \(2017\)](#). For DNNs, there are 225 runs for MLP, 675 runs for MeshNet [Feng et al. \(2019\)](#), 855 runs for GIN [Xu et al. \(2019\)](#), and 540 runs for ExpC [Yang et al. \(2020\)](#), where each setting takes 5

runs of fixed random seeds and 3 ablation studies of different inputs. These detailed experiments can help us dive into the model generalization ability for predicting the particle crushing strength.

Overall, the generalization difficulty of both tasks and methods is examined that DNNs can overcome the difficulty of the Axis task by the non-linearity modeling, and the large prediction variances of GNNs cause its statistical insignificance among different GNNs.

The Axis task is the most difficult task for non-Deep methods, and the Shape task is the most difficult task for DNNs. Existing researches [Huang et al. \(2014\)](#); [Huillca et al. \(2021\)](#); [Fu et al. \(2017\)](#); [Hu et al. \(2022\)](#); [Zhu and Zhao \(2021\)](#); [Sun et al. \(2021\)](#) investigate the effects of the particle crushing strength based on either of the three tasks while neglecting the difficulty comparison between different tasks. Tab. 3 presents that non-Deep methods and DNNs both achieve the least Mean Absolute Error (MAE) and Root Mean Square Error (RMSE) on the Diameter task. On the one hand, the size effect of particle crushing strength has been sufficiently investigated with morphology descriptors. On the other hand, the larger size of particles leads to the degeneration of the strength due to the increasing internal flaws [Huang et al. \(2014\)](#); [Wang et al. \(2021\)](#), as shown in Tab. 2. However, although the maximum strength of the testing set of the Axis task is nearly half of that of the Shape task as shown in Tab. 2, non-Deep methods present significantly larger MAE in the Axis task. In contrast, MLP reduces the MAE by 43.9% on the Axis task compared to XGBoost, the best non-Deep method, based solely on the morphology descriptors, indicating the effective non-linearity modeling of DNNs. ExpC further outperforms MLP by 10.5% with $p = 0.0531$ at the two-sided independent t-test, verifying the usefulness of the fragment graph modeling. The four methods of DNNs obtain higher MAE on the Shape task than that on the Axis task, which is consistent with the testing set distribution as shown in Tab. 2. It indicates that DNNs can better use input morphology descriptors and the fragment graph than non-Deep methods.

MLP outperforms non-Deep methods statistically more significantly. Since

XGBoost and LightGBM are not affected by different random seeds, MLP achieves statistical significance than them on all three tasks and reduces the MAE by 4.8% on the Diameter task, 8.8% on the Shape task, and 43.9% on the Axis task. Furthermore, MLP shares the same morphology descriptors with non-Deep methods, indicating that the particle crushing theory with respect to different conditions requires relational modeling of different aspects, including the geometric, form, roundness, and sphericity descriptors.

ExpC outperforms MLP statistically more significant, but doesn't show statistical significance of other GNNs. Tab. 4 presents that ExpC achieves statistical significance of MLP with the help of the fragment graph and the powerful framework of GNNs. However, although ExpC performs best among GNNs, the p-values of MAE of ExpC and that of other GNNs don't show statistical significance, which is caused by the large variances of other GNNs with different random seeds. It implies a future direction to control the prediction variances of GNNs for predicting the particle crushing strength.

4.2. Ablation Study

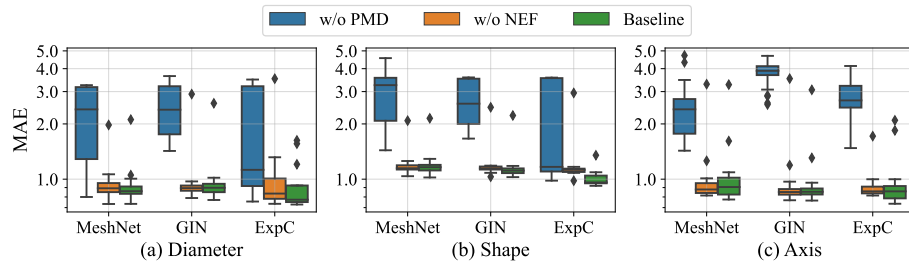


Figure 2: MAE distribution of ablation studies among all parameter settings, including GNNs w/o particle morphology descriptors (PMD), GNNs w/o node and edge features (NEF), and GNNs with both PMD and NEF (Baseline).

The above analysis reveals the superiority of deep learning methods and GNNs, advancing the predictions of particle crushing strength by a large margin. The ablation study aims to investigate the effects of particle morphology descriptors (PMD) and node and edge features (NEF) for GNNs. We further

Table 5: The best performance comparison of ablation studies among all parameter settings, including GNNs w/o particle morphology descriptors (PMD), GNNs w/o node and edge features (NEF), and GNNs with both PMD and NEF (Baseline). The degradation percentages compared to the Baseline are listed here.

Method	Ablation Study	Diameter	Deg. (%)	Shape	Deg. (%)	Axis	Deg. (%)
MeshNet	w/o PMD	0.800 ± 0.044	-11.3	1.506 ± 0.021	-46.6	1.429 ± 0.081	-95.5
	w/o NEF	0.733 ± 0.073	-1.9	1.038 ± 0.108	-1.1	0.815 ± 0.053	-11.5
	Baseline	0.719 ± 0.054	-	1.027 ± 0.046	-	0.731 ± 0.092	-
GIN	w/o PMD	1.425 ± 0.162	-98.2	1.664 ± 0.122	-82.9	2.551 ± 0.286	-242.0
	w/o NEF	0.789 ± 0.028	-9.7	1.030 ± 0.058	-13.2	0.768 ± 0.043	-2.9
	Baseline	0.719 ± 0.083	-	0.910 ± 0.051	-	0.746 ± 0.065	-
ExpC	w/o PMD	0.759 ± 0.072	-7.1	0.982 ± 0.039	-11.2	1.477 ± 0.228	-102.9
	w/o NEF	0.734 ± 0.033	-3.5	0.981 ± 0.070	-11.1	0.815 ± 0.045	-12.0
	Baseline	0.709 ± 0.025	-	0.883 ± 0.036	-	0.728 ± 0.031	-

compute the largest eight distances of a particle fragment to other fragments as the features of node distance and extract the overall largest eight distances as the particle features to complement the PMD and NEF. In this way, *w/o PMD* means removing the PMD or the PMD and the particle distances at the same time, and *w/o NEF* means removing the NEF from GNNs, leaving the features of node distance for GNNs. In summary, PMD has dominated the prediction accuracy of GNNs due to the expert experience [Blott and Pye \(2008\)](#); [Bagheri et al. \(2015\)](#); [Huang et al. \(2020\)](#); [Domokos et al. \(2015\)](#); [Pouranian et al. \(2020\)](#); [Zhao and Wang \(2016\)](#); [Yang et al. \(2017\)](#); [Zheng et al. \(2021\)](#); [Zhang et al. \(2016\)](#), and NEF can further substantially reduce the prediction errors of GNNs consistently on various GNN architectures and the prediction tasks.

Since GNNs exhibit larger variances under different random seeds as shown in Tab. 3, we visualize the variance ranges of GNNs under different parameter settings in Fig. 2 to evaluate the global effects of the PMD and NEF on the hyper-parameter sensitivity of different GNNs on different tasks. Firstly, Fig. 2 shows the significance of PMD that the prediction errors across three tasks increase rapidly with GNNs *w/o PMD*, and the superiority of ExpC that ExpC mostly achieves the best medium performance of the boxplot against two other

methods due to its powerful expressivity [Yang et al. \(2020\)](#). Secondly, PMD reduces the variances of different parameter settings much more than NEF. Thirdly, GNNs equipped with NEF obtain lower MAE than GNNs *w/o NEF* as shown in the MAE distribution, especially on the Shape and Axis tasks of ExpC. It implies that we should identify the task difficulty first and then choose the appropriate GNN architecture.

The best MAE comparison of ablation studies in [Tab. 5](#) obtains consistent results with [Fig. 2](#) that both PMD and NEF reduce the prediction errors of GNNs across the three tasks, and PMD has a much more significant impact than NEF on the three tasks, which are quantitatively verified by the degradation percentages. In contrast to the similar performance of GNNs *w/o NEF* and Baseline in [Fig. 2](#), [Tab. 5](#) provides a more detailed observation that Baseline can improve GNNs *w/o NEF* by up to 13.2% and 12.0% on the Shape and the Axis task, indicating the effectiveness of NEF. Moreover, the best-performing ExpC benefits from NEF consistently across the three tasks. Overall, the ablation studies verified the instability of GNNs without the dedicated PMD and the effectiveness of NEF when applied to GNNs.

4.3. Attribution Analysis

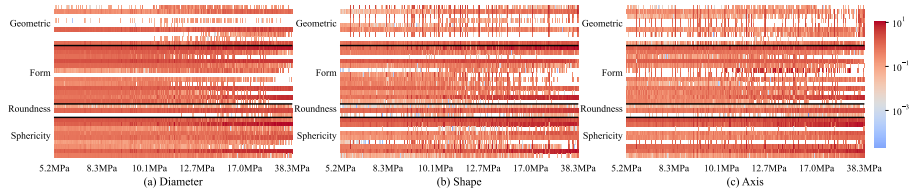


Figure 3: Gradient attribution of the first 34 particle morphology descriptors.

The ablation studies reveal the significance and sensitivity of particle morphology descriptors (PMD) and node and edge features (NEF) with respect to different tasks and GNNs. The attribution analysis aims to understand the detailed mechanisms of PMD and NEF for particle crushing strength prediction with the common patterns and individual patterns of the feature attributions

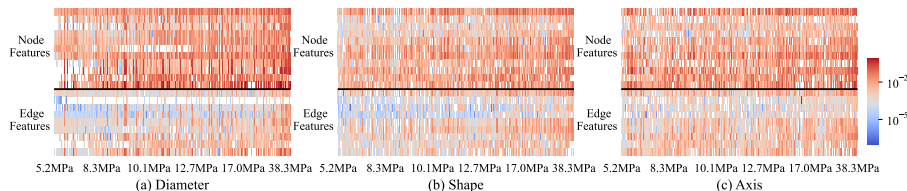


Figure 4: Gradient attribution of node and edge features.

on the three tasks. We adopt the simple yet effective gradient-based method to quantify the impacts of inputs for the predictions, which has been employed from CNNs Song et al. (2019); Feng et al. (2022) to GNNs Jing et al. (2021). We choose the ExpC with its best-performing hyper-parameters as shown in Tab. 3 and fix its random seed as 0 to obtain the trained model. Let \hat{y} be the prediction strength of a particle and \mathbf{x} be the input PMD and NEF, and we average the magnitudes of gradient attributions for a specific particle type, written as $\frac{1}{|\mathbf{X}_{type}|} \sum_{\mathbf{x} \in \mathbf{X}_{type}} |\frac{\partial \hat{y}}{\partial \mathbf{x}}|$, where \mathbf{X}_{type} is a particle type with the specific diameter, shape, and axis. The attribution distributions of PMD and NEF are visualized in Fig. 3 and Fig. 4, where the X-axis represents the true particle strength from 5.09 MPa to 38.29 MPa, including the training set, the validation set and the testing set to eliminate the differences of the testing sets of the three tasks and discover the common and individual patterns of the attribution distributions.

We remove the 35-th PMD of the stability descriptor since its small attributions degrade the visualization effects, which is provided in Fig. C.9. The first 34 PMD are divided into four groups as shown in Fig. 3, *e.g.* Geometric, Form, Roundness, and Sphericity. The highlighted horizontal bars shown in Fig. 3 summarize the common patterns of the three tasks that only partial features of different groups provide impressive attributions. On the one hand, it is caused by the similarity and redundancy of different descriptors. On the other hand, the simulation particles exhibit the standard spheroidicity with specified shape factors rather than realistic particles with various shapes Wang et al. (2021); Ma et al. (2022), which limits the effectiveness of morphology descriptors. Besides the common patterns, the sparse vertical bars occur more frequently on

the Shape and the Axis task than on the Diameter task, which is consistent with the task difficulty as shown in Tab. 3 that a difficult task requires more complex relationships between different descriptors. The horizontal and vertical bars can point out the effectiveness and the cooperative relationships of PMD on the three tasks.

NEF contain the local descriptors of particle fragments and their interactive faces. As depicted in Fig. 4, the attribution distributions of NEF exhibit significantly smaller values than those of PMD. This difference can be attributed to the hierarchical aggregation mechanism of ExpC, which aggregates the small attributions to large attributions, and the higher significance of PMD in the hybrid framework, as shown in Tab. 5. Although the node features provide more attributions than the edge features, the node features exhibit larger attributions from the Diameter task to the Shape and Axis task, while the edge features exhibit the contrary trend. It implies that the interactions of fragments can well model the particle crushing behaviors with the *state-of-the-art* GNNs on the more difficult tasks. It will be a promising direction to explore the interactions of fragments during particle crushing in future work.

5. Discussion

Existing researches have developed various statistical theories like Weibull statistics $P_s(V_0) = \exp\left[-\left(\frac{\sigma}{\sigma_0}\right)^m\right]$ and machine learning methods to characterize the size effects Sun et al. (2021); Hu et al. (2022) and morphology effects Wang et al. (2021); Ma et al. (2022) of particle crushing. However, since particle crushing occurs in various civil engineering fields Xiao et al. (2020), GNNs with the fragment graph, as constitutive modeling, can largely alleviate the efforts to predict the particle crushing strength more accurately and attribute the prediction contributions more efficiently. We summarize the limitations and future works as follows.

More realistic simulations. We generate the particle crushing dataset following Hu et al. Hu et al. (2022), which varies the diameter, shape, and axis as

shown in Tab. 1. Nonetheless, the dataset mainly consists of particles with the standard spheroidicity, which deviate largely from the realistic particle shapes Sun et al. (2021); Wang et al. (2021); Ma et al. (2022). Besides, the uniaxial compression is employed to simplify the loading condition in the particle crushing process, while the triaxial test Hu et al. (2022) and different loading conditions can be explored in the future.

More powerful GNNs for particle crushing. We test the generalization ability of these *state-of-the-art* GNNs by reducing the learning difficulty of GNNs based on the dedicated PMD features Wang et al. (2021), which leaves space for improvements. For example, the interactions of fragments during loading can be modeled by GNNs to explore the detailed behaviors of particle crushing in different time steps. Besides, it is necessary to consider the external loading conditions when introducing more realistic simulations.

Quantitative attributions of features. We explain the feature attributions based on the quantitative gradient-based methods Song et al. (2019); Jing et al. (2021); Feng et al. (2022). However, the common and individual patterns of different tasks are qualitatively summarized to highlight the contributions of different features. It requires cooperation with civil engineering researchers to iteratively identify the significant descriptors and predict the particle crushing strength with GNNs.

6. Conclusion

In this paper, we are motivated by the lack of a large-scale dataset on particle crushing and the successful applications of GNNs to propose a method to predict particle crushing strength based on fragment connectivity. Experimental results demonstrate the effectiveness of a hybrid framework that combines MLP and GNNs, and surprisingly show the comparable performance of three different GNNs, namely MeshNet Feng et al. (2019), GIN Xu et al. (2019), and ExpC Yang et al. (2020). The significantly improved performance motivates further exploration of particle crushing under different conditions, such

as variations in particle diameters, shapes, and compression axes. Our analysis reveals the importance and sensitivity of particle morphology descriptors and features of GNNs in generalizing to different tasks. Nonetheless, in everyday use of granular materials, various compression conditions require more comprehensive modeling of particle crushing. In the future, we aim to explore the use of Graph Neural Networks (GNNs) with improved connectivity to predict particle crushing based on a more comprehensive modeling approach.

Appendix A. Particle Crushing Dataset

Figure A.5 describes the load-displacement curve of a randomly sampled particle, where the peak force decreases drastically due to the particle breakage during the external load. We strictly follow the instructions of Hu *et al.* Hu et al. (2022) to perform a batch of simulations of 45,000 particles, adopting the Non-Smooth Contact Dynamics (NSCD) method for the numerical simulations of particle crushing. The parameters of the Cohesive Zone Model (CZM) of the NSCD method are also calibrated by Hu *et al.* Hu et al. (2022). After generating the comprehensive dataset, we filter particles without at least 35% decrease Wang et al. (2021); Huilca et al. (2021); Hu et al. (2022) from the peak force since these particles aren't considered to break into pieces, and compute the characteristic particle crushing strength σ_0 of 900 particle types, where the particle types without more than 30 valid simulations McDowell and Amon (2000); Hu et al. (2022) of particle crushing are further removed to ensure the data sufficiency for the fitted Weibull distribution. Finally, we have obtained 40,818 valid data points and 882 particle types of particle crushing.

Appendix A.1. Compression Test of Single Particle

Particle meshing. The software Neper Quey et al. (2011) provides the Voronoi tessellation of a sphericity particle, whose diameter, three-dimensional scale coefficients, and rotation angles are given as the input parameters of Neper. The different diameters, shapes, and compression axes of our dataset are firstly

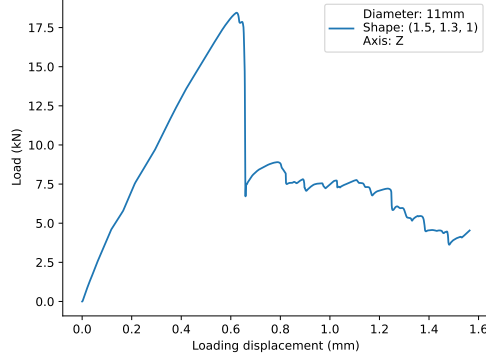


Figure A.5: The load-displacement curve in a particle compression test.

Table A.6: Parameters for the cohesive zone model.

$K_I(\text{N}/\text{mm}^3)$	$K_{II}(\text{N}/\text{mm}^3)$	$\sigma_f^e(\text{MPa})$	$\sigma_{II}^e(\text{MPa})$	$G_I(\text{mJ}/\text{mm}^2)$	$G_{II}(\text{mJ}/\text{mm}^2)$	μ	$\rho(\text{kg}/\text{m}^3)$
80	120	9	11.5	900	1125	0.3	2650

introduced in the particle meshing process. The Voronoi tessellation divides the specified polyhedral particle into multiple convex cells, simulating the fragment distribution of the particle and the common faces of different fragments. A Voronoi cell can be defined as follows [Cantor et al. \(2017\)](#)

$$V_i = \{x \in \mathbf{X} \mid d(x, P_i) < d(x, P_j) \forall j \neq i\}, \quad (\text{A.1})$$

where \mathbf{X} is the three-dimensional point set of the particle space, P_i and P_j are the given points of the i -th and j -th cell. The final output of Voronoi tessellation is optimized by iteratively replacing the given points P_i, P_j with their new centroids c_i, c_j until convergence [Cantor et al. \(2017\)](#). Gmsh [Geuzaine and Remacle \(2009\)](#) further produces a meshing of the particle based on the `geo` file generated by Neper. We have also obtained the `tess` file generated by Neper for the convenience of modelling the fragments and their contacts in a fragment graph.

Numerical simulation. We perform numerical simulations of the NSCD method by LMG90 [Dubois and Mozul \(2013\)](#) after generating the mesh files

of 45,000 particles. The meshing particle with a specified rotation axis is assumed to be compressed along the new Z-axis by two parallel platens. The NSCD method [Jean \(1999\)](#); [Jean and Moreau \(1992\)](#); [Moreau \(1988\)](#) updates the displacement of each element at each time step by detecting the contacts and computing the contact forces between bodies, following the Signorini-Coulomb condition for a unilateral contact. The unilateral Signorini condition describes the non-penetrability between two objects, written as follows

$$\begin{cases} v_n > 0 & \Rightarrow f_n = 0, \\ v_n = 0 & \Rightarrow f_n \geq 0, \end{cases} \quad (\text{A.2})$$

where v_n is the relative velocity between particles in the normal direction, and f_n is the contact force in the normal direction. The contact force f_t in the tangential direction obeys the Coulomb friction law, written as

$$\begin{cases} v_t > 0 & \Rightarrow f_t = -\mu f_n, \\ v_t = 0 & \Rightarrow -\mu f_n \leq f_t \leq \mu f_n, \\ v_t < 0 & \Rightarrow f_t = \mu f_n, \end{cases} \quad (\text{A.3})$$

where μ is the contact friction coefficient between particles and is set as 0.3 in our simulations. The CZM model [Camacho and Ortiz \(1996\)](#); [Hu et al. \(2022\)](#) quantifies the relationship between breakage energy and the maximum displacement of the breakage of the contact faces, whose parameters are determined based on the work of [Hu et al. \(2022\)](#).

Appendix A.2. Weibull Distribution For Particle Crushing

[McDowell et al. \(2000\)](#) have found that the particle crushing strength of geometrically similar particles follows a Weibull distribution, written as

$$P_s = \exp \left[- \left(\frac{d_s}{d_0} \right)^3 \left(\frac{\sigma}{\sigma_0} \right)^m \right], \quad (\text{A.4})$$

where P_s is the breakage ratios under the corresponding load, d_0 and σ_0 are the characteristic diameter and crushing strength, respectively. The survival probability of a batch of 50 particles with the same geometry is drawn in [Fig. A.6](#),

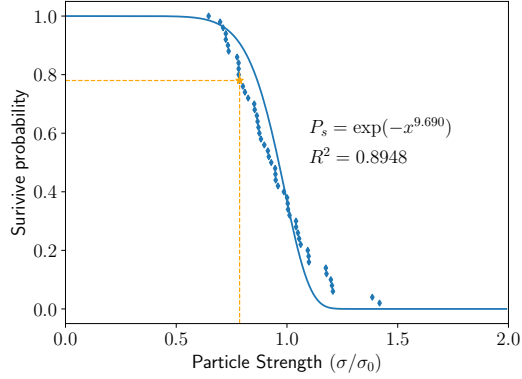


Figure A.6: 50 particle crushing data points and the fitting Weibull distribution of crushing strength. The particle type and the highlighted data point are both the same with Fig. A.5.

sorting by the normalized particle strength, where $m = 9.690$ is the Weibull modulus and indicates the variability of the particle crushing distribution. The characteristic particle strength is thus scaled to 1.0 of the horizontal axis, and corresponds to the 37% survival probability of the vertical axis. Existing particle crushing theories [McDowell and Amon \(2000\)](#); [Sun et al. \(2021\)](#); [Wang et al. \(2021\)](#) derive a close-form formula to describe the size effects of particles with different diameters. However, firstly, their various theories have been proposed from different perspectives and lacked the consensus of the particle crushing behaviors. Secondly, our experimental results of the non-Deep methods and DNNs in Tab. 3 reveal that particle morphology descriptors play a vital role on the generalization of predicting the particle crushing strength, while existing theories are mostly based on the particle diameter. Thirdly, generalizing the predictions for more conditions like the particle shapes and compression axes require a constitutive model to describe the particle from different viewpoints. Therefore, we are motivated to model the fragment connection of the particle with Graph Neural Networks (GNNs), which offer a natural modelling for the fragment graph.

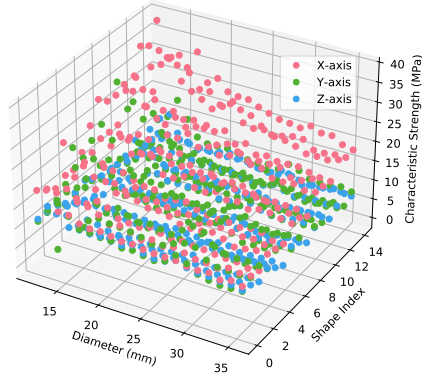


Figure A.7: The characteristic particle crushing strength with respect to different diameters, shapes and compression axes.

Table A.7: The distribution of the characteristic strength (σ_0) and Weibull modulus m of the dataset.

	min	25%	50%	75%	max
σ_0 (MPa)	5.09	8.65	11.03	15.06	38.29
m	0.69	3.88	5.54	6.86	11.60

Appendix A.3. Dataset Statistics

In the particle generation stage, we have chosen 900 particle types, which is the Cartesian product of 20 particle diameters, 15 scale shapes in the (X, Y, Z) axes, and 3 compression axes, as shown in Tab. 1. We have conducted 50 numerical simulations with random Voronoi tessellation for each particle type to ensure the data sufficiency to measure the characteristic crushing strength. Firstly, we reserve the particles that can be observed at least 35% decrease Wang et al. (2021); Huilca et al. (2021); Hu et al. (2022) from the peak force to ensure the particle breakage. Secondly, we remove particle types that contain less than 30 valid simulations McDowell and Amon (2000); Hu et al. (2022) from our dataset to ensure the data quality. As stated before, we have obtained 882 particle types and 40,818 particles finally.

Tab. A.7 describes that 882 particle types present smooth variations in terms

of the characteristic strength σ_0 and the Weibull modulus m , which is consistent with observations from Sun et al. (2021); Hu et al. (2022). Moreover, the outliers of the particle types are centered around the maximum values, where the maximum values are around two times larger than the 75% percentile of σ_0 and m . It poses significant challenges to the machine learning methods. Fig. A.7 visualizes the distribution of σ_0 in terms of three different conditions, including the diameter, shape and compression axis. Firstly, the compression axis increases σ_0 more significantly than the other two conditions, which may be attributed to that the scale coefficient of the X-axis is larger than the Y-axis and Z-axis as shown in Tab. 1. Secondly, the outliers of the 882 particle types are centered in the corner of the 3D plot, which presents small diameter, flat shape and the X-axis. We believe that the comprehensive dataset can sufficiently reveal the diversity of particle crushing behaviors and benchmark the machine learning methods for particle crushing.

Appendix A.4. Particle Features

We have calculated thirty-five Particle Morphology Descriptors (PMD) according to the work of Wang et al. Wang et al. (2021), as shown in Fig. A.8. The feature distributions can be roughly categorized into three kinds: the uniform distribution (e.g., Shortest Length), the long-tail distribution (e.g., Volume), and the Gaussian distribution (e.g., Diameter of the maximum inscribed sphere). It is noteworthy that the distributions of the flatness (Form 11) and the sphericity (Sphericity 8) are significantly different from the Gaussian distribution of that Wang et al. (2021), which is caused between the differences of simulated particles and natural particles. The diverse feature distributions also verify that it is rather difficult to predict particle crushing strength only based on the diameter feature.

We have also developed eleven node features to describe each fragment of the particle and nine edge features for the connectivity between fragments, as shown in Tab. A.8. These features also present similar distributions to the PMD since they share similar definitions with PMD. The particular advantage of node

Table A.8: Feature components of node features and edge features, where (3) means three variables.

Features	Details
Node Features	Volume(1), Surface Area(1), Diameter(1), Number of Faces(1), Number of Neighbors(1), Centroid Coordinates(3), Euler Angles(3)
Edge Features	Contact Area(1), Number of Lines(1), Maximum Length of the Contact Area(1), Centroid Coordinates(3), Euler Angles(3)

features and edge features is that they can describe the microscopic behaviors of fragments beyond the overall behaviors of the particle.

Appendix B. Graph Neural Networks for Particle Crushing

Appendix B.1. Graph Neural Networks

Graph Neural Networks (GNNs) have shown its powerful prediction abilities on the non-grid data and been applied to various fields such as Recommendation [Ying et al. \(2018\)](#), traffic flow prediction [Yu et al. \(2018\)](#), and molecular classification [Gilmer et al. \(2017\)](#); [Xu et al. \(2019\)](#); [Yang et al. \(2020\)](#); [Ying et al. \(2021\)](#). A graph is defined by a node set $V = \{v_1, \dots, v_n\}$ and an associated edge set $E = \{e_1, \dots, e_m\}$, where e_1 connects a pair of adjacent fragments v_i and v_j . The message-passing paradigm [Gilmer et al. \(2017\)](#) describes GNNs in a microscopic view that each node v_i receives the messages from its neighbors $v_j \in \mathcal{N}(v_i)$ and updates its representation based on these messages, written as:

$$\begin{aligned} \mathbf{m}_i^k &= \sum_{v_j \in \mathcal{N}(v_i)} \mathbf{M}_k(\mathbf{h}_i^k, \mathbf{h}_j^k, \mathbf{e}_{ij}), \\ \mathbf{h}_i^{k+1} &= \mathbf{U}_k(h_i^k, \mathbf{m}_i^k), \end{aligned} \tag{B.1}$$

where v_i updates from \mathbf{h}_i^k of the k -th layer to \mathbf{h}_i^{k+1} of $k + 1$ -th layer based on the message function \mathbf{M}_k and the update function \mathbf{U}_k . The obtained node representation \mathbf{h}_i can be used for various tasks such as node classification [Kipf](#)

and Welling (2017) and link prediction Ying et al. (2018). It requires a readout function to generate a representation vector for the whole graph G for graph-level tasks like molecular classification Gilmer et al. (2017); Xu et al. (2019); Yang et al. (2020); Ying et al. (2021), written as

$$\mathbf{h}_G = \mathbf{R}(\{\mathbf{h}_i^K | v_i \in V\}), \quad (\text{B.2})$$

where K is the number of neural network layers.

We have adopted MeshNet Feng et al. (2019), GIN Xu et al. (2019), and ExpC Yang et al. (2020) as our baseline GNNs for particle crushing. We have also tried the powerful Graphormer Ying et al. (2021), which has achieved the first place together with ExpC Yang et al. (2020) in the PCQM4M-LSC track of KDD Cup 2021 ⁵, but failed the memory requirements on our GPU of 24GB Titan X. These three GNNs can be summarized as follows:

- MeshNet Feng et al. (2019) is called a Convolutional Neural Network for meshing files, by aggregating neighborhood information based on its spatial descriptor and structural descriptor and pooling the overall representation. The working mechanism of MeshNet Feng et al. (2019) exactly meets the definition of the message-passing paradigm Gilmer et al. (2017) and implements the readout function with a global average pooling layer. Therefore, MeshNet is considered as a variant of GNNs in this paper.
- GIN Xu et al. (2019) is proposed as a more powerful GNNs to discriminate the isomorphism graph better by building an injective mapping from neighborhood message to node representations, innovatively leading a new direction of enhancing the discriminative power of GNNs.
- ExpC Yang et al. (2020) improves the expressive power of GNNs beyond 1-WL test based on the innovative ExpandingConv and CombConv. Ying et al. Ying et al. (2021) have achieved the first place in the PCQM4M-

⁵<https://ogb.stanford.edu/kddcup2021/results/#awardees-pcqm4m>

LSC track of KDD Cup 2021 by combing Graphormer [Ying et al. \(2021\)](#) and ExpC [Yang et al. \(2020\)](#).

Appendix B.2. Predicting Particle Crushing Strength

The crushing behavior of a particle is closely related with the particle shape and the internal structure, as shown in previous theoretical studies [McDowell and Bolton \(1998\)](#); [Daouadji et al. \(2001\)](#); [Russell and Khalili \(2004\)](#); [Tengattini et al. \(2016\)](#). Numerical simulations of various particles have become the mostly adopted method to study the relations between the particle and its crushing strength since experimental tests are costly and unscalable [Cheng et al. \(2004\)](#); [de Bono and McDowell \(2014\)](#); [Fu et al. \(2017\)](#). In a numerical simulation, a particle is divided into multiple rigid polyhedral cells randomly [Nguyen et al. \(2015\)](#) and gets fractured during the compression test [Hu et al. \(2022\)](#). The crushing strength of the particle reveals its internal characteristic, benefiting for various engineering fields including geotechnical engineering, mining, chemical engineering, and so on [Zhu and Zhao \(2019a\)](#).

From the perspective of machine learning, the tessellated particle can be seen as a connected graph, where each polyhedral cell plays as a node. Formally, the cell set is denoted by $V = \{v_1, \dots, v_i, \dots, v_n\}$, where v_i refers to a polyhedral cell and n denotes the number of cells. A node v_i is usually associated with a node vector \mathbf{v}_i to describe the node states, as listed in Tab. A.8. The edges of the *internal graph* are formed according to the spatial proximity of each cell pair. The edge set of the internal graph is denoted by $E = \{e_1, \dots, e_m\}$, where e_1 connects two in-contact (adjacent) cells v_i and v_j . An edge e_k could also carry the relational vector \mathbf{e}_k of the two cells, such as the contact surface areas and the angle of the contact [Vlassis et al. \(2020\)](#). Our task is predicting the particle crushing strength on particles of unseen types with the help of GNNs [Feng et al. \(2019\)](#); [Xu et al. \(2019\)](#); [Yang et al. \(2020\)](#), given the internal graph $G = \{V, E\}$ and its associated vectors $\mathbf{x} = \{\{\mathbf{v}_i | \forall v_i \in V\}, \{\mathbf{e}_k | \forall e_k \text{ in } E\}\}$. The problem can

Table C.9: Grid search of parameters of machine learning methods.

Method	Parameter	Settings
Linear	Default	Default
Ridge	alpha	[1e-3, 1e-2, 1e-1, 1.0]
Random Forest	n_estimators	[10, 25, 50, 75, 100]
	min_samples_split	[2, 8, 32]
	criterion	[squared_error, absolute_error, poisson]
LightGBM	n_estimators	[10, 25, 50, 75, 100]
	max_depth	[4, 16, 64]
	reg_alpha	[0.0, 1e-3, 1e-2, 1e-1, 1.0]
	reg_lambda	[0.0, 1e-3, 1e-2, 1e-1, 1.0]
XGBoost	n_estimators	[10, 25, 50, 75, 100]
	max_depth	[4, 16, 64]
	reg_alpha	[0.0, 1e-3, 1e-2, 1e-1, 1.0]
	reg_lambda	[0.0, 1e-3, 1e-2, 1e-1, 1.0]

be formulated as

$$\arg \min_{\mathbf{g}} \sum_{\mathbf{x} \in \mathbf{X}, \mathbf{y} \in \mathbf{Y}} \|\mathbf{y} - \mathbf{g}(\mathbf{x}, G)\|_2 + \lambda \Omega(\mathbf{g}), \quad (\text{B.3})$$

where \mathbf{g} is one kind of GNNs and Ω is the regularization term.

Appendix C. Experiment Settings

We have obtained three testing sets by splitting the dataset according to the diameters, scale shapes, and compression axes to examine the generalization ability of different methods across three tasks. The testing sets are split around 1/3 as shown in Tab. 1, where 7/20 for the diameter task, 5/15 for the shape task, and 1/3 for the axis task.

Appendix C.1. Hyper-parameters

We have conducted experiments with five non-Deep methods, including Linear Regression, Ridge Regression, Random Forest, LightGBM [Ke et al. \(2017\)](#),

Table C.10: Default parameters of deep learning methods.

Method	Default Parameters			
MLP	batch_size=128, dropout=1e-1	learning_rate=1e-3,	hidden=128,	layers=2,
MeshNet	batch_size=128, dropout=1e-1	learning_rate=1e-3,	hidden=128,	layers=2,
GIN	batch_size=128, dropout=1e-1, eps=1e-5, JK=max	learning_rate=1e-3,	hidden=128,	layers=2,
ExpC	batch_size=128, dropout=1e-1, head_size=32	learning_rate=1e-3,	hidden=128,	layers=2,

and XGBoost [Chen and Guestrin \(2016\)](#), and four DNNs, including MLP, MeshNet [Feng et al. \(2019\)](#), GIN [Xu et al. \(2019\)](#), and ExpC [Yang et al. \(2020\)](#). For a fair comparison, we have tried our best to grid search the hyper-parameters for non-Deep methods, as shown in Tab. C.9. The experimental results of non-Deep methods verify the effectiveness of them based on the dedicated particle morphology descriptors. Since the computation cost of DNNs is much larger than that of non-Deep methods, we firstly determine a group of parameters according to our experience as shown in Tab. C.10. Particularly, the number of ExpC layers is set to 2 to avoid the Out-Of-Memory error on our GPU. Then, we iteratively replace the default parameter with one parameter shown in Tab. C.11. We have conducted five runs for each kind of parameter combination. In summary, we have conducted at least 15 runs for Linear Regression, 60 runs for Ridge Regression, 675 runs for Random Forest, 5625 runs for LightGBM, and 5625 runs for XGBoost across three tasks. We have further performed three kinds of ablation studies for DNNs, resulting in 675 runs for MLP, 675 runs for MeshNet, 855 runs for GIN, and 540 runs for ExpC. These experiments can largely reduce the variances of different methods and ensure a fair comparison.

Table C.11: Iterative search of parameters of deep learning methods.

Method	Parameter	Settings
MLP	batch_size	[8, 32, 128, 512]
	learning_rate	[1e-5, 1e-4, 1e-3, 1e-2]
	hidden	[128, 256, 512]
	layers	[2, 3, 4, 5]
MeshNet	batch_size	[8, 32, 128, 512]
	learning_rate	[1e-5, 1e-4, 1e-3, 1e-2]
	hidden	[128, 256, 512]
	layers	[2, 3, 4, 5]
GIN	batch_size	[8, 32, 128, 512]
	learning_rate	[1e-5, 1e-4, 1e-3, 1e-2]
	hidden	[128, 256, 512]
	layers	[2, 3, 4, 5]
	JK	[last, cat, max, lstm]
ExpC	batch_size	[8, 32, 128, 512]
	learning_rate	[1e-5, 1e-4, 1e-3, 1e-2]
	hidden	[128, 256, 512]
	layers	[2]

Appendix C.2. More results of Attribution Analysis

As shown in Fig. C.9, the 35-th PMD of the stability descriptor presents the smallest attributions with respect to different particle crushing strength, resulting in low contrast of different descriptors. It can be observed from Fig. C.9 that the light and dark colors differ from each other significantly across the X-axis, which can be used for feature importance directly to remove less useful descriptors. However, it poses challenges to compare the attribution analysis across the X-axis and three tasks.

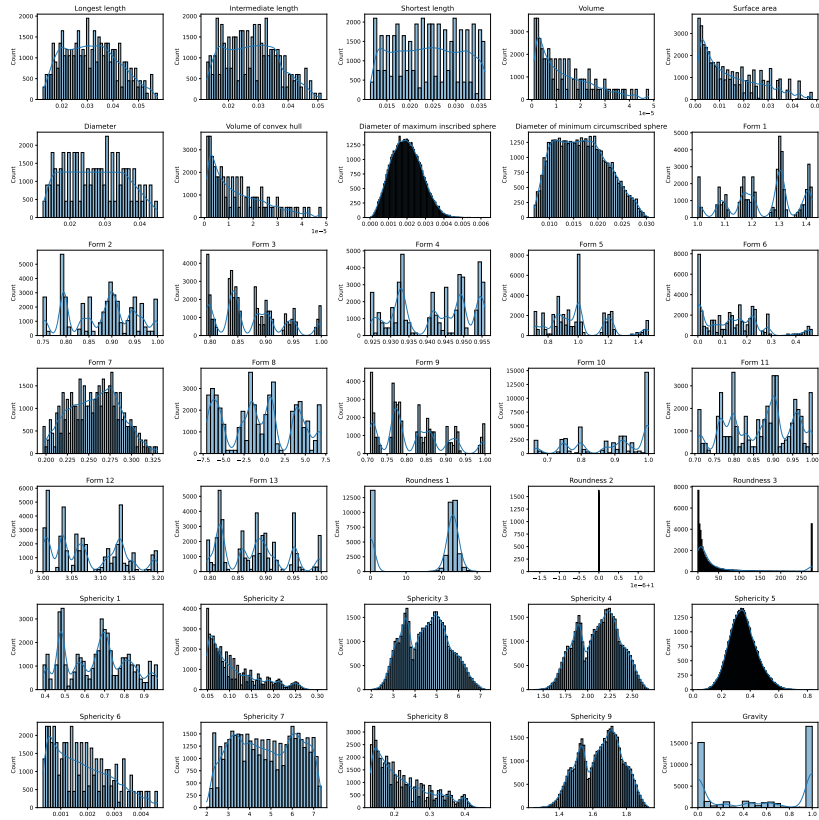


Figure A.8: The distribution of 35 Particle Morphology Descriptors (PMD) Wang et al. (2021), including 9 geometric characteristics Wang et al. (2021), 13 form descriptors Blott and Pye (2008); Bagheri et al. (2015); Huang et al. (2020); Domokos et al. (2015), 3 roundness descriptors Pouranian et al. (2020); Huang et al. (2020); Zhao and Wang (2016), 9 sphericity descriptors Blott and Pye (2008); Pouranian et al. (2020); Yang et al. (2017); Zheng et al. (2021); Huang et al. (2020); Zhang et al. (2016), and 1 instability descriptor Wang et al. (2021).

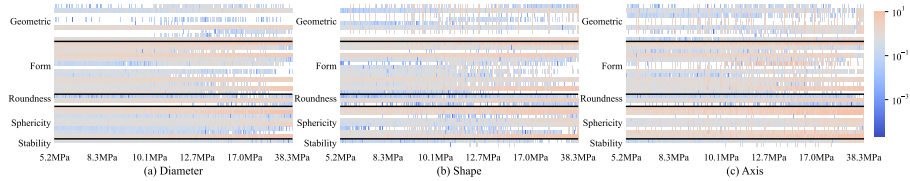


Figure C.9: Gradient attribution of particle morphology descriptors.

References

- Addanki R, Battaglia P, Budden D, Deac A, Godwin J, Keck T, Li WLS, Sanchez-Gonzalez A, Stott J, Thakoor S, Veličković P. Large-scale graph representation learning with very deep gnns and self-supervision. arXiv preprint arXiv:210709422 2021;.
- Bagheri G, Bonadonna C, Manzella I, Vonlanthen P. On the characterization of size and shape of irregular particles. *Powder Technology* 2015;270:141–53.
- Blott SJ, Pye K. Particle shape: a review and new methods of characterization and classification. *Sedimentology* 2008;55(1):31–63.
- de Bono JP, McDowell GR. Dem of triaxial tests on crushable sand. *Granular Matter* 2014;16(4):551–62.
- Bronstein MM, Bruna J, LeCun Y, Szlam A, Vandergheynst P. Geometric deep learning: going beyond euclidean data. *IEEE Signal Processing Magazine* 2017;34(4):18–42.
- Camacho GT, Ortiz M. Computational modelling of impact damage in brittle materials. *International Journal of solids and structures* 1996;33(20-22):2899–938.
- Cantor D, Azéma E, Sornay P, Radjai F. Three-dimensional bonded-cell model for grain fragmentation. *Computational Particle Mechanics* 2017;4(4):441–50.
- Chang KH, Cheng CY. Learning to simulate and design for structural engineering. In: *International Conference on Machine Learning*. PMLR; 2020. p. 1426–36.
- Chang S, Pierson E, Koh PW, Gerardin J, Redbird B, Grusky D, Leskovec J. Mobility network models of covid-19 explain inequities and inform reopening. *Nature* 2021;589(7840):82–7.

- Chen T, Guestrin C. Xgboost: A scalable tree boosting system. In: Proceedings of the 22nd acm sigkdd international conference on knowledge discovery and data mining. 2016. p. 785–94.
- Cheng Y, Bolton M, Nakata Y. Crushing and plastic deformation of soils simulated using dem. *Geotechnique* 2004;54(2):131–41.
- Daouadji A, Hicher PY, Rahma A. An elastoplastic model for granular materials taking into account grain breakage. *European Journal of Mechanics-A/Solids* 2001;20(1):113–37.
- Domokos G, Kun F, Sipos AA, Szabó T. Universality of fragment shapes. *Scientific reports* 2015;5(1):9147.
- Dubois F, Mozul R. Lmgc90. In: 11e colloque national en calcul des structures. 2013. .
- Feng Y, Feng Y, You H, Zhao X, Gao Y. Meshnet: Mesh neural network for 3d shape representation. In: Proceedings of the AAAI Conference on Artificial Intelligence. volume 33; 2019. p. 8279–86.
- Feng Z, Hu J, Wu S, Yu X, Song J, Song M. Model doctor: A simple gradient aggregation strategy for diagnosing and treating cnn classifiers. In: Proceedings of the AAAI Conference on Artificial Intelligence. volume 36; 2022. p. 616–24.
- Fu R, Hu X, Zhou B. Discrete element modeling of crushable sands considering realistic particle shape effect. *Computers and Geotechnics* 2017;91:179–91.
- Geuzaine C, Remacle JF. Gmsh: A 3-d finite element mesh generator with built-in pre-and post-processing facilities. *International journal for numerical methods in engineering* 2009;79(11):1309–31.
- Gilmer J, Schoenholz SS, Riley PF, Vinyals O, Dahl GE. Neural message passing for quantum chemistry. In: International conference on machine learning. PMLR; 2017. p. 1263–72.

- Griffith AA. Vi. the phenomena of rupture and flow in solids. Philosophical transactions of the royal society of london Series A, containing papers of a mathematical or physical character 1921;221(582-593):163–98.
- Hardin BO, et al. Crushing of soil particles. Journal of geotechnical engineering 1985;111(10):1177–92.
- Hu S, Guo N, Yang Z, Zhao J. Implicit dem analyses of the size and shape effects on the crushing strength of rockfill particles. Chinese Journal of Geotechnical Engineering 2022;:1–9.
- Huang J, Xu S, Yi H, Hu S. Size effect on the compression breakage strengths of glass particles. Powder Technology 2014;268:86–94.
- Huang Q, Zhou W, Ma G, Ng TT, Xu K. Experimental and numerical investigation of weibullian behavior of grain crushing strength. Geoscience Frontiers 2020;11(2):401–11.
- Huillca Y, Silva M, Ovalle C, Quezada JC, Carrasco S, Villavicencio GE. Modelling size effect on rock aggregates strength using a dem bonded-cell model. Acta Geotechnica 2021;16(3):699–709.
- Jean M. The non-smooth contact dynamics method. Computer methods in applied mechanics and engineering 1999;177(3-4):235–57.
- Jean M, Moreau JJ. Unilaterality and dry friction in the dynamics of rigid body collections. In: 1st Contact Mechanics International Symposium. 1992. p. 31–48.
- Jiang H, Meng D. 3d numerical modelling of rock fracture with a hybrid finite and cohesive element method. Engineering Fracture Mechanics 2018;199:280–93.
- Jing Y, Yang Y, Wang X, Song M, Tao D. Amalgamating knowledge from heterogeneous graph neural networks. In: Proceedings of the IEEE/CVF conference on computer vision and pattern recognition. 2021. p. 15709–18.

- Ke G, Meng Q, Finley T, Wang T, Chen W, Ma W, Ye Q, Liu TY. Lightgbm: A highly efficient gradient boosting decision tree. *Advances in neural information processing systems* 2017;30.
- Kipf TN, Welling M. Semi-supervised classification with graph convolutional networks. In: *International Conference on Learning Representations*. 2017. .
- Kun F, Herrmann HJ. A study of fragmentation processes using a discrete element method. *Computer Methods in Applied Mechanics and Engineering* 1996;138(1-4):3–18.
- Lade PV, Yamamuro JA, Bopp PA. Significance of particle crushing in granular materials. *Journal of Geotechnical Engineering* 1996;122(4).
- LeCun Y, Bengio Y, Hinton G. Deep learning. *nature* 2015;521(7553):436–44.
- Ma G, Wang Y, Zhou H, Lu X, Zhou W. Morphology characteristics of the fragments produced by rock grain crushing. *International Journal of Geomechanics* 2022;22(4):04022020.
- Ma G, Zhou W, Chang XL. Modeling the particle breakage of rockfill materials with the cohesive crack model. *Computers and Geotechnics* 2014;61:132–43.
- McDowell G, Amon A. The application of weibull statistics to the fracture of soil particles. *Soils and foundations* 2000;40(5):133–41.
- McDowell G, Bolton M. On the micromechanics of crushable aggregates. *Géotechnique* 1998;48(5):667–79.
- Moreau JJ. Unilateral contact and dry friction in finite freedom dynamics. *Nonsmooth mechanics and Applications* 1988;:1–82.
- Nader F, Silvani C, Djeran-Maigre I. Effect of micro and macro parameters in 3d modeling of grain crushing. *Acta Geotechnica* 2019;14(6):1669–84.
- Nakata A, Hyde M, Hyodo H, Murata . A probabilistic approach to sand particle crushing in the triaxial test. *Géotechnique* 1999;49(5):567–83.

- Nguyen DH, Azéma E, Sornay P, Radjai F. Bonded-cell model for particle fracture. *Physical Review E* 2015;91(2):022203.
- Ovalle C, Frossard E, Dano C, Hu W, Maiolino S, Hicher PY. The effect of size on the strength of coarse rock aggregates and large rockfill samples through experimental data. *Acta Mechanica* 2014;225(8):2199–216.
- Page L, Brin S, Motwani R, Winograd T. The pagerank citation ranking: Bringing order to the web. Technical Report; Stanford InfoLab; 1999.
- Pedregosa F, Varoquaux G, Gramfort A, Michel V, Thirion B, Grisel O, Blondel M, Prettenhofer P, Weiss R, Dubourg V, et al. Scikit-learn: Machine learning in python. *the Journal of machine Learning research* 2011;12:2825–30.
- Pouranian MR, Shishehbor M, Haddock JE. Impact of the coarse aggregate shape parameters on compaction characteristics of asphalt mixtures. *Powder Technology* 2020;363:369–86.
- Quey R, Dawson P, Barbe F. Large-scale 3d random polycrystals for the finite element method: Generation, meshing and remeshing. *Computer Methods in Applied Mechanics and Engineering* 2011;200(17-20):1729–45.
- Rafiee A, Gasc-Barbier M, Vinches M. Stochastic model generation for discontinuous rock mass media and numerical analysis using the nscd method (case study: Saint-bé at gallery in the southwest of france). In: 12th ISRM Congress. OnePetro; 2011. .
- Rafiee A, Vinches M, Bohatier C. Modelling and analysis of the nîmes arena and the arles aqueduct subjected to a seismic loading, using the non-smooth contact dynamics method. *Engineering Structures* 2008;30(12):3457–67.
- Russell AR, Khalili N. A bounding surface plasticity model for sands exhibiting particle crushing. *Canadian Geotechnical Journal* 2004;41(6):1179–92.
- Schulte-Sasse R, Budach S, Hnisz D, Marsico A. Integration of multiomics data with graph convolutional networks to identify new cancer genes and their

- associated molecular mechanisms. *Nature Machine Intelligence* 2021;3(6):513–26.
- Song J, Chen Y, Wang X, Shen C, Song M. Deep model transferability from attribution maps. *Advances in Neural Information Processing Systems* 2019;32.
- Sun Z, Ma G, Zhou W, Han W, Yuan C, Bin X. Influence of particle shape on size effect of crushing strength of rockfill particles. *Rock and Soil Mechanics* 2021;42(2):430–8.
- Tengattini A, Das A, Einav I. A constitutive modelling framework predicting critical state in sand undergoing crushing and dilation. *Géotechnique* 2016;66(9):695–710.
- Vlassis NN, Ma R, Sun W. Geometric deep learning for computational mechanics part i: Anisotropic hyperelasticity. *Computer Methods in Applied Mechanics and Engineering* 2020;371:113299.
- Wang Y, Ma G, Mei J, Zou Y, Zhang D, Zhou W, Cao X. Machine learning reveals the influences of grain morphology on grain crushing strength. *Acta Geotechnica* 2021;16(11):3617–30.
- Xiao Y, Desai CS, Daouadji A, Stuedlein AW, Liu H, Abuel-Naga H. Grain crushing in geoscience materials—key issues on crushing response, measurement and modeling: Review and preface. *Geoscience Frontiers* 2020;11(2):363–74.
- Xu K, Hu W, Leskovec J, Jegelka S. How powerful are graph neural networks? In: *International Conference on Learning Representations*. 2019. URL: <https://openreview.net/forum?id=ryGs6iA5Km>.
- Yang M, Shen Y, Qi H, Yin B. Breaking the expressive bottlenecks of graph neural networks. *arXiv preprint arXiv:201207219* 2020;.
- Yang Y, Cheng YM, Sun Q. The effects of rolling resistance and non-convex particle on the mechanics of the undrained granular assemblies in 2d. *Powder Technology* 2017;318:528–42.

- Ying C, Cai T, Luo S, Zheng S, Ke G, He D, Shen Y, Liu TY. Do transformers really perform badly for graph representation? *Advances in Neural Information Processing Systems* 2021;34:28877–88.
- Ying R, He R, Chen K, Eksombatchai P, Hamilton WL, Leskovec J. Graph convolutional neural networks for web-scale recommender systems. In: *Proceedings of the 24th ACM SIGKDD international conference on knowledge discovery & data mining*. 2018. p. 974–83.
- Yu B, Yin H, Zhu Z. Spatio-temporal graph convolutional networks: a deep learning framework for traffic forecasting. In: *Proceedings of the 27th International Joint Conference on Artificial Intelligence*. 2018. p. 3634–40.
- Yu Y, Yin J. Energy dissipation properties of three gorges granite under different loading modes. *Chin J Rock Mech Eng* 2004;23(2):205–8.
- Zhang J, Ye J, Chen J, Li S. A preliminary study of measurement and evaluation of breakstone grain shape. *Rock and Soil Mechanics* 2016;37(2):343–8.
- Zhang S, Liu L, Gao S, He D, Fang X, Li W, Huang Z, Su W, Wang W. Litegem: Lite geometry enhanced molecular representation learning for quantum property prediction. 2021. [arXiv:2106.14494](https://arxiv.org/abs/2106.14494).
- Zhang Z, Xu M, Jamasb A, Chenthamarakshan V, Lozano A, Das P, Tang J. Protein representation learning by geometric structure pretraining. In: *International Conference on Learning Representations*. 2023. .
- Zhao B, Wang J. 3d quantitative shape analysis on form, roundness, and compactness with μct . *Powder technology* 2016;291:262–75.
- Zheng J, He H, Alimohammadi H. Three-dimensional wadell roundness for particle angularity characterization of granular soils. *Acta Geotechnica* 2021;16:133–49.
- Zhu F, Zhao J. Modeling continuous grain crushing in granular media: a hybrid peridynamics and physics engine approach. *Computer Methods in Applied Mechanics and Engineering* 2019a;348:334–55.

Zhu F, Zhao J. A peridynamic investigation on crushing of sand particles. *Géotechnique* 2019b;69(6):526–40.

Zhu F, Zhao J. Interplays between particle shape and particle breakage in confined continuous crushing of granular media. *Powder Technology* 2021;378:455–67.